

Multiscale Induction Machine Modeling in the dq0 Domain Including Main Flux Saturation

Yue Xia , Ying Chen, Hua Ye , and Kai Strunz 

Abstract—In this paper, a multiscale induction machine model for the simulation of diverse transients in power systems is developed in the dq0 domain. The proposed model includes main flux saturation. The equations that describe the electrical performance of the induction machine are represented through analytic signals whose Fourier spectrum can be shifted. In addition to the time-step size, the shift frequency appears as a novel simulation parameter. When the shift frequency is set to zero, then the model processes instantaneous signals for the representation of natural waveforms. When the shift frequency is set to the frequency of the stator electrical quantities in the dq reference frame, the Fourier spectra of the analytic signals are shifted to become dynamic phasors that allow for efficient envelope tracking. The setting of the shift frequency is adapted to the transients observed during simulation. Test cases verify the proposed multiscale saturable induction machine model and show that it supports accurate and efficient simulation of both electromagnetic and electromechanical transients within a simulation run.

Index Terms—Dynamic phasor, electromagnetic transients, electromechanical transients, induction machine, main flux saturation, multiscale, shift frequency.

I. INTRODUCTION

ELECTROMAGNETIC transients programs (EMTP) are widely used to simulate electromagnetic transients in power system, wherein instantaneous signals are processed to track the natural waveforms [1]–[3]. The computational efficiency of EMTP is reduced when the Fourier spectra of the natural waveforms are concentrated around the carrier frequency, which is either 50 or 60 Hz in power systems. Algorithms that process dynamic phasor signals to track envelope waveforms are used for efficient simulation of electromechanical transients [4]–[7]. Based on the generalized averaging method [8], the dynamic phasors are defined as the time-varying Fourier coefficients of the natural waveforms. If it is of interest

to study both electromagnetic and electromechanical transients within the same study, then the concept of frequency-adaptive simulation of transients (FAST) [9]–[11] offers an efficient solution. It is distinguished by introducing an adjustable simulation parameter called the shift frequency in addition to the time-step size. The virtues of simulation in the time domain as in EMTP and dynamic phasor calculus are combined due to the use of analytic signals. Accurate and efficient multi-scale simulation is so supported. The application of the shift frequency with the objective to obtain dynamic phasors is also referred to as shifted-frequency analysis (SFA) and has shown to give efficient simulations [12]–[14].

This paper focuses on the modeling of saturable induction machines for multi-scale simulation. Generally, in the modeling of induction machinery, the application of the dq0 transform has been popular. The magnetic saturation may be readily included in the dq0 model [15]. However, when to be connected to network models represented in the abc phase domain, the dq0 models do have indirect interfaces. A small time-step size is required to accurately represent the saturation phenomenon and to keep the interfacing error under certain tolerance [16]. As an alternative to the dq0 model, the phase domain (PD) induction machine model for EMTP was introduced in [17] to provide a direct machine-network interface. However, the representation of magnetic saturation using PD formulation is more complex than that in the dq0 model [18]. In [19], [20], the voltage-behind-reactance (VBR) induction machine model including magnetic saturation and also offering direct machine-network interfacing was proposed. A relatively large time-step size may be used in the VBR induction machine model to represent the saturation phenomenon. The time-step size, however, is still limited by numerical accuracy considerations in EMTP-type simulation [19]. It is insufficient to support efficient simulation of electromechanical transients.

To enhance the computational efficiency of the simulation during electromechanical transients, frequency shifting is applied to the PD induction machine model in [21]. The electrical quantities are described through dynamic phasor calculus. The dynamic phasors allow for larger time-step sizes in representing electromechanical transients compared with the original EMTP-type solution of [1]. In [22], frequency shifting is applied to the VBR induction machine model, the model is expressed using a state-space formulation. The electrical quantities are treated the same way as is done with phasor representation of electrical quantities in [21]. This model is therefore suited for the simulation of electromechanical transients. However, the models

Manuscript received November 30, 2017; revised April 26, 2018 and July 9, 2018; accepted July 18, 2018. Date of publication August 2, 2018; date of current version May 2, 2019. This work was supported by the National Key Research and Development Plan of China (2018YFB0904500). Paper no. TEC-00913-2017. (Corresponding author: Yue Xia.)

Y. Xia and Y. Chen are with the Department of Electrical Engineering and Applied Electronic Technology, Tsinghua University, Beijing 100084, China (e-mail: xiayuexia@163.com; chen_ying@tsinghua.edu.cn).

H. Ye is with the Institute of Electrical Engineering, Chinese Academy of Sciences, Beijing 100190, China (e-mail: yehua@mail.iee.ac.cn).

K. Strunz is with the SENSE Laboratory, Department of Electrical Engineering and Computer Sciences, Technische Universität Berlin, Berlin 10587, Germany (e-mail: kai.strunz@tu-berlin.de).

Color versions of one or more of the figures in this paper are available online at <http://ieeexplore.ieee.org>.

Digital Object Identifier 10.1109/TEC.2018.2863101

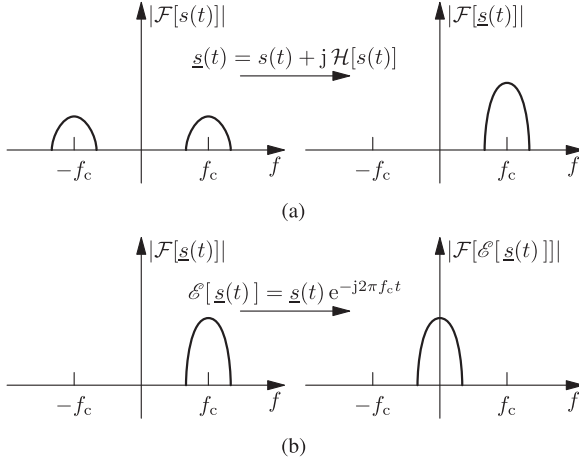


Fig. 1. Analytic signal processing and frequency shifting [9]. (a) Application of the Hilbert transform. (b) Shifting by the carrier frequency.

in [21], [22] do not account for flux saturation. While saturation effects are important, the assumption that the induction machine is a linear device is an oversimplification that is not suited for the study of the behavior of induction machines in all modes of operation [23].

The work presented in this paper resulted in a multi-scale induction machine model that supports the integrative simulation of diverse transients from the steady state to high frequencies with multiple time-steps as well as saturation. The contributions made in this paper are mainly threefold. Firstly, the electromagnetic equations of the induction machine in the dq0 domain are represented through analytic signals comprising real and imaginary parts. The main flux saturation is considered. The prediction of magnetic saturation and the interface between the dq0 induction machine model and the remainder of the network model are improved. Secondly, the shift frequency is introduced as an adjustable parameter in the induction machine model and is adapted to the situation given by the prevailing transients in the simulation. Thirdly, case studies of a single-machine system, a multi-machine system, and a machine controlled by a voltage-sourced converter (VSC)-based drive system are carried out to validate the proposed model in terms of accuracy and efficiency across different time scales.

In Section II, the key characteristics of analytic signals are reviewed. In Section III, a multi-scale saturable induction machine model based on FAST is formulated. In Section IV, the proposed induction machine model is applied and validated. Conclusions are drawn in Section V.

II. SHIFT FREQUENCY IN SIMULATION

Naturally generated signals $s(t)$ are real. The Hilbert transform can be used to create a quadrature component that is added as an imaginary part to obtain the corresponding analytic signal denoted through an underscore [24]:

$$\underline{s}(t) = s(t) + j\mathcal{H}[s(t)]. \quad (1)$$

The effect of the creation of the analytic signal from an original bandpass signal $s(t)$ of carrier frequency f_c is shown in Fig. 1(a). While the Fourier spectrum of $s(t)$ extends to negative

frequencies, this is not the case for the corresponding analytic signal $\underline{s}(t)$. Therefore, the analytic signal $\underline{s}(t)$ can be shifted by the so-called shift frequency f_s :

$$\mathcal{S}[\underline{s}(t)] = \underline{s}(t)e^{-j2\pi f_s t}. \quad (2)$$

If the shift frequency is set equal to the carrier frequency $f_s = f_c$, then the complex envelope $\mathcal{E}[\underline{s}(t)]$ is obtained as shown in Fig. 1(b). Since $|e^{-j2\pi f_s t}| = 1$, the magnitude is not changed through the shift operation. The complex envelope is a low-pass signal whose maximum frequency is lower than the one of the original real bandpass signal. Thus, a larger time-step size can be chosen when tracking the complex envelope rather than the original bandpass signal according to Shannon's sampling theory [25]. If the shift frequency f_s is set to zero, then the real parts of the analytic signals are used, and the natural waveforms are tracked at small time-step sizes as in EMTP-type simulation. For the multi-scale simulation, both shift frequency and time-step size are adjusted adaptively. Details on the selection of shift frequency and time-step size are discussed in [9].

III. MULTISCALE SATURABLE INDUCTION MACHINE MODELING

In accordance with [23], a three-phase symmetrical induction machine is assumed with the stator and rotor windings respectively being identical, sinusoidally distributed and separated by 120° . Without loss of generality, only main flux saturation is considered. This assumption has been used in many papers [19], [20], and readers may refer to [20] provided for a detailed discussion of this assumption. Furthermore, the stator and rotor leakage flux saturation can be readily included using the same approach described in the paper. The aim of this section is to develop a multi-scale model of a three-phase induction machine that considers main flux saturation. In a first modeling step, continuous machine equations represented through instantaneous signals in the dq0 domain are given in Section III-A. Then, three reference frames are introduced in Section III-B. In Section III-C, multi-scale machine equations in the dq0 domain are discretized. In Section III-D, the method of representation of magnetic saturation is described. In Section III-E, the integration of machine and network equations is discussed. The discretized mechanical equations of the multi-scale saturable induction machine model are given in Section III-F. The implementation of the multi-scale saturable induction machine model is described in Section III-G. Finally, the machine-network solution is given in Section III-H.

A. Continuous Machine Equations in dq0 Domain

Referring to [23], the voltage equations of a symmetrical induction machine in dq0 domain may be written as follows:

$$v_{dq}(t) = \frac{d}{dt}\lambda_{dq}(t) + \mathbf{R}i_{dq}(t) - \omega\lambda_{dq}(t), \quad (3)$$

$$v_{0s}(t) = R_s i_{0s}(t) + \frac{d\lambda_{0s}(t)}{dt}, \quad (4)$$

$$v_{0r}(t) = R_r i_{0r}(t) + \frac{d\lambda_{0r}(t)}{dt}, \quad (5)$$

with

$$\boldsymbol{\lambda}_{dq}(t) = (\lambda_{ds}(t), \lambda_{qs}(t), \lambda_{dr}(t), \lambda_{qr}(t))^T, \quad (6)$$

$$\mathbf{v}_{dq}(t) = (v_{ds}(t), v_{qs}(t), v_{dr}(t), v_{qr}(t))^T, \quad (7)$$

$$\mathbf{i}_{dq}(t) = (i_{ds}(t), i_{qs}(t), i_{dr}(t), i_{qr}(t))^T, \quad (8)$$

$$\mathbf{R} = \text{diag}(R_s, R_s, R_r, R_r), \quad (9)$$

$$\boldsymbol{\omega} = \begin{bmatrix} 0 & \omega & 0 & 0 \\ -\omega & 0 & 0 & 0 \\ 0 & 0 & 0 & \omega - \omega_r \\ 0 & 0 & -(\omega - \omega_r) & 0 \end{bmatrix}, \quad (10)$$

where $v_{ds}(t)$, $v_{qs}(t)$ and $v_{0s}(t)$ are the direct, quadrature and zero sequence components of the stator voltages, respectively; $v_{dr}(t)$, $v_{qr}(t)$ and $v_{0r}(t)$ are the respective components of the rotor voltages; in the special case of a squirrel-cage rotor, the rotor voltages $v_{dr}(t) = 0$ V, $v_{qr}(t) = 0$ V [26]; $i_{ds}(t)$, $i_{qs}(t)$ and $i_{0s}(t)$ are the direct, quadrature and zero sequence components of the stator currents, respectively; $i_{dr}(t)$, $i_{qr}(t)$ and $i_{0r}(t)$ are the respective components of the rotor currents; $\lambda_{ds}(t)$, $\lambda_{qs}(t)$ and $\lambda_{0s}(t)$ are the direct, quadrature and zero sequence components of the stator fluxes, respectively; $\lambda_{dr}(t)$, $\lambda_{qr}(t)$ and $\lambda_{0r}(t)$ are the respective components of the rotor fluxes; R_s and R_r are constant stator and rotor resistances, respectively; ω is the rotational speed of the reference frame as applied to the stationary circuit; ω_r is the electrical rotor angular speed. The derivation of (3) is given in Appendix A.

The flux linkages $\boldsymbol{\lambda}_{dq}(t)$, $\lambda_{0s}(t)$ and $\lambda_{0r}(t)$ may be expressed as [23]:

$$\boldsymbol{\lambda}_{dq}(t) = \mathbf{L}\mathbf{i}_{dq}(t), \quad (11)$$

$$\lambda_{0s}(t) = L_{ls}i_{0s}(t), \quad (12)$$

$$\lambda_{0r}(t) = L_{lr}i_{0r}(t), \quad (13)$$

with

$$\mathbf{L} = \begin{bmatrix} L_{ls} + L_m & 0 & L_m & 0 \\ 0 & L_{ls} + L_m & 0 & L_m \\ L_m & 0 & L_{lr} + L_m & 0 \\ 0 & L_m & 0 & L_{lr} + L_m \end{bmatrix}, \quad (14)$$

where L_{ls} and L_{lr} represent the stator and rotor leakage inductances, respectively; L_m denotes the magnetizing inductance. The derivation of (11) is given in Appendix A.

Insertion of (11) into (3) gives:

$$\frac{d}{dt}\boldsymbol{\lambda}_{dq}(t) = \mathbf{v}_{dq}(t) + (\boldsymbol{\omega} - \mathbf{R}\mathbf{L}^{-1})\boldsymbol{\lambda}_{dq}(t). \quad (15)$$

The equation of motion is given by:

$$\frac{d\omega_r(t)}{dt} = \frac{p}{2J}(T_e(t) - T_m(t)), \quad (16)$$

$$\frac{d\theta_r(t)}{dt} = \omega_r(t), \quad (17)$$

TABLE I
SPEED OF ROTATION AND CARRIER FREQUENCY OF dq
COMPONENTS IN DIFFERENT REFERENCE FRAMES

Reference frame	Reference frame speed ω	Carrier frequency f_c
Rotor	ω_r	$(\omega_e - \omega_r)/2\pi$
Stationary	0 rad/s	50 Hz or 60 Hz
Synchronous	ω_e	0 Hz

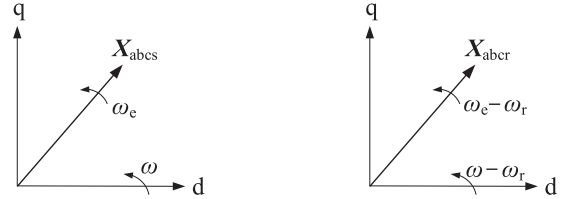


Fig. 2. Phasor representation for the variables associated with the stator and rotor circuits; left: stator circuit; right: rotor circuit.

where $\theta_r(t)$ is the rotor angle; J is the machine inertia; p is the number of poles; $T_m(t)$ and $T_e(t)$ are the mechanical and electromagnetic torques, respectively. The electromagnetic torque is expressed in the dq0 domain as [23]:

$$T_e(t) = \frac{3p}{4}(\lambda_{ds}(t)i_{qs}(t) - \lambda_{qs}(t)i_{ds}(t)). \quad (18)$$

B. Three Reference Frames

The electrical equations of an induction machine may be expressed in dq-coordinates with different reference frames such as the stationary frame, the rotor frame, or the synchronous frame [23]. The voltage equation for each of these reference frames may be obtained from (3) by assigning the appropriate speed of the rotation of the reference frame to ω in $\boldsymbol{\omega}$ (10). The values of ω for different reference frames are listed in Table I; that is, $\omega = 0$ rad/s for the stationary, $\omega = \omega_r$ for the rotor, and $\omega = \omega_e$ for the synchronous reference frame. Variable ω_e is the ac carrier angular speed in the abc phase domain, which is typically either 314 rad/s for a 50 Hz system or 377 rad/s for a 60 Hz system. By a reference frame transformation, the three-phase abc components are transformed to the specific reference frame. Fig. 2 shows the phasor diagram of the variables \mathbf{X}_{abcs} and \mathbf{X}_{abcr} , which represent voltage, current, or flux, in the stator and rotor circuits, respectively. The stator variable \mathbf{X}_{abcs} in the three-phase abc frame has a carrier frequency which is typically either 50 or 60 Hz. While the rotor variable \mathbf{X}_{abcr} has a slip frequency which is equal to $(\omega_e - \omega_r)/2\pi$. The reference frame associated with the stator circuit rotates at the angular speed of ω , the reference frame associated with the rotor circuit rotates at the angular speed of $\omega - \omega_r$. When the variables \mathbf{X}_{abcs} and \mathbf{X}_{abcr} are represented in dq-coordinates, the dq components of \mathbf{X}_{abcs} and \mathbf{X}_{abcr} have a special carrier frequency. The value of such special carrier frequency depends on the chosen reference frame. The relationships between the reference frame and carrier frequency of dq components are given in Table I.

C. Formulation of Multiscale Discretized Machine Equations in dq0 Domain

For multi-scale simulation, the machine model is to be able to deal with instantaneous and dynamic phasor signals at the network interface. All time-variant quantities are represented through analytic signals to allow for frequency shifting as reviewed in Section II. The differential equation (15) is expressed through analytic signals as follows:

$$\frac{d}{dt} \underline{\lambda}_{dq}(t) = \underline{v}_{dq}(t) + (\omega - \mathbf{RL}^{-1}) \underline{\lambda}_{dq}(t). \quad (19)$$

Multiplying both sides of (19) by $e^{-j\omega_s t}$, application of the product rule of differentiation, and introduction of the notation of (2) to represent the operation of frequency shifting yields:

$$\begin{aligned} \left(j\omega_s + \frac{d}{dt} \right) \mathcal{S} [\underline{\lambda}_{dq}(t)] &= \mathcal{S} [\underline{v}_{dq}(t)] \\ &+ (\omega - \mathbf{RL}^{-1}) \mathcal{S} [\underline{\lambda}_{dq}(t)], \end{aligned} \quad (20)$$

where $\omega_s = 2\pi f_s$. The shift frequency is arbitrary, two settings of the shift frequency are of particular significance. In the unshifted case of $f_s = 0$ Hz, the representation is made with instantaneous signals. Taking the real part on both sides gives (15). Thus, this situation is suitable for the tracking of natural waveforms of instantaneous signals as used in the EMTP. In the shifted case where the shift frequency is made equal to the carrier frequency given in Table I: $f_s = f_c$, the equations are represented with shifted analytic signals. This situation is suitable for the tracking of envelopes as done when processing dynamic phasors.

For consistency of the overall approach, the equations (4), (5) and (11) are also represented using analytic signals:

$$\underline{v}_{0s}(t) = R_s \dot{i}_{0s}(t) + \frac{d\underline{\lambda}_{0s}(t)}{dt}, \quad (21)$$

$$\underline{v}_{0r}(t) = R_r \dot{i}_{0r}(t) + \frac{d\underline{\lambda}_{0r}(t)}{dt}, \quad (22)$$

$$\underline{\lambda}_{dq}(t) = \mathbf{L} \underline{i}_{dq}(t). \quad (23)$$

Application of the trapezoidal integration method to transform (20) into a difference equation leads to:

$$\begin{aligned} j\omega_s \frac{\mathcal{S} [\underline{\lambda}_{dq}(k)] + \mathcal{S} [\underline{\lambda}_{dq}(k-1)]}{2} + \frac{\mathcal{S} [\underline{\lambda}_{dq}(k)] - \mathcal{S} [\underline{\lambda}_{dq}(k-1)]}{\tau} \\ = \frac{\mathcal{S} [\underline{v}_{dq}(k)] + \mathcal{S} [\underline{v}_{dq}(k-1)]}{2} \\ + (\omega - \mathbf{RL}^{-1}) \frac{\mathcal{S} [\underline{\lambda}_{dq}(k)] + \mathcal{S} [\underline{\lambda}_{dq}(k-1)]}{2}, \end{aligned} \quad (24)$$

where τ is the time-step size, and k is the time-step counter.

By inserting analytic signals as in [9], (24) is rearranged as follows:

$$\underline{\lambda}_{dq}(k) = \underline{\mathbf{F}} \underline{v}_{dq}(k) + \underline{\boldsymbol{\eta}}(k) \quad (25)$$

with

$$\underline{\mathbf{F}} = \frac{\tau}{2} \left(\left(1 + \frac{j\omega_s \tau}{2} \right) \mathbf{I} - (\omega - \mathbf{RL}^{-1}) \frac{\tau}{2} \right)^{-1} \quad (26)$$

$$\begin{aligned} \underline{\boldsymbol{\eta}}(k) &= \frac{2}{\tau} \underline{\mathbf{F}} \left[\frac{\tau}{2} e^{j\omega_s \tau} \underline{v}_{dq}(k-1) \right. \\ &\left. + e^{j\omega_s \tau} \left(\left(1 - \frac{j\omega_s \tau}{2} \right) \mathbf{I} + (\omega - \mathbf{RL}^{-1}) \right) \underline{\lambda}_{dq}(k-1) \right], \end{aligned} \quad (27)$$

where \mathbf{I} is the identity matrix, $\underline{\mathbf{F}}$ is defined as the feedforward term, and $\underline{\boldsymbol{\eta}}$ is defined as the history term. It should be noted that the voltage $\underline{v}_{dq}(k)$ at the step k is unknown when calculating $\underline{\lambda}_{dq}(k)$ in (25). In this paper, $\underline{v}_{dq}(k)$ is predicted through the voltage at the previous step as follows:

$$\tilde{\underline{v}}_{dq}(k) = e^{j\omega_c \tau} \underline{v}_{dq}(k-1), \quad (28)$$

where $\omega_c = 2\pi f_c$, f_c is the frequency of the voltage \underline{v}_{dq} . As shown in Section III-B, the value of f_c depends on the chosen reference frame and is given in Table I. Throughout this paper, the symbol “ \sim ” indicates predicted values. When electromagnetic transients are studied, a very small time-step size τ is used, the term $e^{j\omega_c \tau}$ is therefore very small. The voltage \underline{v}_{dq} at step k can be predicted by the voltage at the previous step. When electromechanical transients are studied at much larger time-step sizes, the terminal voltages are expected to retain their sinusoidal shape, the following relation applies: $\underline{v}_{dq}(k-1) e^{j\omega_c \tau} \approx \underline{v}_{dq}(k)$. In steady state, $\underline{v}_{dq}(k-1) e^{j\omega_c \tau} = \underline{v}_{dq}(k)$. Hence, the prediction in (28) is reasonable. An example is given in Appendix V-B to show the quality of prediction with analytic signals.

When $\underline{\lambda}_{dq}(k)$ is calculated by using (25), the current $\underline{i}_{dq}(k)$ is obtained according to (23):

$$\underline{i}_{dq}(k) = \mathbf{L}^{-1} \underline{\lambda}_{dq}(k). \quad (29)$$

Application of the trapezoidal method to transform (21) into difference equation and rearranging leads to:

$$\begin{aligned} \dot{i}_{0s}(k) &= \frac{\tau}{2L_{1s} + \tau R_s} (\underline{v}_{0s}(k) + \underline{v}_{0s}(k-1)) \\ &+ \frac{2L_{1s} - \tau R_s}{2L_{1s} + \tau R_s} \dot{i}_{0s}(k-1). \end{aligned} \quad (30)$$

Equations (29) and (30) yield the output current \dot{i}_{dq0s} in dq0 coordinates. The three-phase output current \dot{i}_{Mabc} is obtained by the back reference frame transformation:

$$\dot{i}_{Mabc}(k) = \mathbf{K}^{-1} \dot{i}_{dq0s}(k). \quad (31)$$

where \mathbf{K} performs transformations of stator quantities to the specific reference frame shown in Section III-B. The transformation is given in Appendix V-C.

D. Representation of Magnetic Saturation

The saturation curve which may be represented by nonlinear functions [17], [27] or piecewise-linear functions [19], [20] is widely used to represent the main flux saturation. A typical saturation curve of an induction machine is shown in Fig. 3

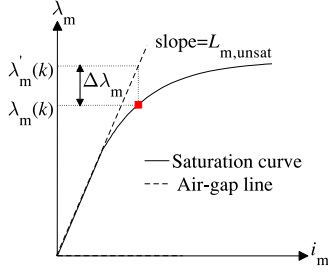


Fig. 3. Representation of saturation characteristic.

along with the air-gap line. The saturation curve is obtained from the main flux versus magnetizing current. The departure of the saturation curve from the air-gap line is an indication of the degree of saturation. The effect of saturation may be represented as [27]:

$$L_m = K_{\text{sat}} L_{m,\text{unsat}}, \quad (32)$$

where $L_{m,\text{unsat}}$ is the unsaturated value of magnetizing inductance, the value of $L_{m,\text{unsat}}$ is equal to the slope of the air-gap line, K_{sat} is the saturation factor which identifies the degree of saturation. The magnetizing inductance L_m varies with magnetic saturation. Referring to Fig. 3, for an operating point on the saturation curve which is marked by square, the saturation factor K_{sat} is given by [26], [27]

$$K_{\text{sat}} = \frac{\lambda_m(k)}{\lambda'_m(k)}, \quad (33)$$

or

$$K_{\text{sat}} = \frac{\lambda_m(k)}{\lambda_m(k) + \Delta\lambda_m}, \quad (34)$$

where λ_m denotes the main flux.

For multi-scale simulation, λ_m is expressed in terms of the direct and quadrature components as follows [23]:

$$\lambda_m(k) = \sqrt{(\text{Re}[\underline{\lambda}_{md}(k)])^2 + (\text{Re}[\underline{\lambda}_{mq}(k)])^2}, \quad (35)$$

where “Re” is used to denote the real part of analytic signal, the variables $\underline{\lambda}_{md}(t)$ and $\underline{\lambda}_{mq}(t)$ are the direct and quadrature components of the main flux, respectively. They are represented by using analytic signals:

$$\underline{\lambda}_{md}(k) = L_m (\underline{i}_{ds}(k) + \underline{i}_{dr}(k)), \quad (36)$$

$$\underline{\lambda}_{mq}(k) = L_m (\underline{i}_{qs}(k) + \underline{i}_{qr}(k)). \quad (37)$$

As shown in (32) and (33), the magnetizing inductance L_m is related to the saturation factor K_{sat} while K_{sat} is associated with the main flux linkage $\lambda_m(k)$. This implies that the magnetizing inductance L_m at time-step k is dependent on the main flux linkage $\lambda_m(k)$ at time-step k which is unknown. Therefore, a prediction of $\lambda_m(k)$ is required to compute L_m . The prediction consists of the following steps.

- By using analytic signals instead of real signals, the values of $\underline{\lambda}_{md}(k)$ and $\underline{\lambda}_{mq}(k)$ are predicted through the values at the previous step:

$$\tilde{\underline{\lambda}}_{md}(k) = e^{j\omega_e \tau} \underline{\lambda}_{md}(k-1), \quad (38)$$

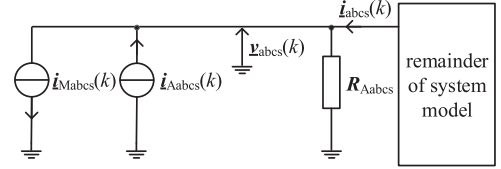


Fig. 4. Network interfacing of induction machine model.

$$\tilde{\underline{\lambda}}_{mq}(k) = e^{j\omega_e \tau} \underline{\lambda}_{mq}(k-1). \quad (39)$$

Unlike the linear prediction, the predictions in (38) and (39) allow the use of large time-step sizes during electromechanical transients or steady state. The reader may refer to a similar prediction in (28) for a more detailed explanation. In Appendix V-B, the quality of prediction with analytic signals is shown by comparison with the linear prediction.

- With the predicted values of $\tilde{\underline{\lambda}}_{md}(k)$ and $\tilde{\underline{\lambda}}_{mq}(k)$, the predicted main flux $\tilde{\lambda}_m(k)$ is computed by using (35).

E. Machine-Network Interfacing

The induction machine model described in Section III-C is in fact a voltage-controlled current source. The injected current $\underline{i}_{Mabcs}(k)$ at time-step k is dependent on past terminal voltages $\underline{v}_{abcs}(k-1)$. To prevent the machine from being totally open circuited and attain a stable interface, an adjustment current source $\underline{i}_{Aabcs}(k)$ and an adjustment three-phase resistance \underline{R}_{Aabcs} are placed from the machine terminals to ground [2]. The interface is illustrated in Fig. 4. The proposed interface is designed for efficient multi-scale integrative simulation of electromagnetic and electromechanical transients of induction machines. A similar interface used for the multi-scale synchronous machine is presented in [10], [28]. The resistance per phase R_A of \underline{R}_{Aabcs} is chosen to reflect the characteristic impedance. For an induction machine, this characteristic impedance is chosen as the total leakage impedance [2]. The per-phase resistance R_A of \underline{R}_{Aabcs} is given by

$$R_A = \frac{L_{ls} + L_{lr}}{\tau}. \quad (40)$$

The three-phase resistance matrix \underline{R}_{Aabcs} is given by:

$$\underline{R}_{Aabcs} = \text{diag}(R_A, R_A, R_A). \quad (41)$$

The adjustment current source $\underline{i}_{Aabcs}(k)$ is determined as:

$$\underline{i}_{Aabcs}(k) = \frac{\underline{v}_{abcs}(k-1) e^{j\omega_e \tau}}{R_A}. \quad (42)$$

Instead of injecting the calculated machine current $\underline{i}_{Mabcs}(k)$, the actual current $\underline{i}_{abcs}(k)$ injected into the network is

$$\underline{i}_{abcs}(k) = \underline{i}_{Mabcs}(k) + \frac{\underline{v}_{abcs}(k) - \underline{v}_{abcs}(k-1) e^{j\omega_e \tau}}{R_A}. \quad (43)$$

The third term of (43) is defined as adjust term. The stator voltage $\underline{v}_{abcs}(k)$ may be predicted by $\underline{v}_{abcs}(k-1) e^{j\omega_e \tau}$, this prediction is similar to the one presented in (28) and [10]. Therefore, the adjustment term is very small independent of the time-step

size. The interface allows the characteristic resistance R_A to be seen from the network for sudden voltage changes.

F. Formulation of Mechanical Equations

Real parts of the analytic signals are used to calculate the electromagnetic torque:

$$T_e(k) = \frac{3p}{4} (\text{Re}[\underline{\lambda}_{ds}(k)] \text{Re}[\underline{i}_{qs}(k)] - \text{Re}[\underline{\lambda}_{qs}(k)] \text{Re}[\underline{i}_{ds}(k)]). \quad (44)$$

The mechanical system of (16) and (17) is discretized as follows:

$$\omega_r(k) = \omega_r(k-1) + \frac{p}{2} \frac{\tau}{J} (T_e(k) + T_e(k-1) - T_m(k) - T_m(k-1)), \quad (45)$$

$$\theta_r(k) = \theta_r(k-1) + \frac{\tau}{2} (\omega_r(k) + \omega_r(k-1)). \quad (46)$$

G. Implementation of Multiscale Induction Machine Model

For the purpose of discussion of the machine implementation procedure, the proposed multi-scale model is assumed to be connected to a network. It is assumed that the voltages $\underline{v}_{abcs}(k-1)$ are known to the multi-scale model. They are provided by the system model solver covering the network. The algorithm of the multi-scale model is given as follows.

- 1) Get the machine terminal voltages $\underline{v}_{abcs}(k-1)$ from the system model solver. The machine terminal voltages are used as inputs to the multi-scale model.
- 2) Predict the electrical rotor speed $\tilde{\omega}_r(k)$ using linear extrapolation:

$$\tilde{\omega}_r(k) = 2\omega_r(k-1) - \omega_r(k-2). \quad (47)$$

- 3) Predict $\tilde{\lambda}_{md}(k)$ and $\tilde{\lambda}_{mq}(k)$ using (38) and (39).
- 4) Calculate the magnetizing flux $\tilde{\lambda}_m(k)$ using (35).
- 5) Calculate the saturation factor K_{sat} using the predicted flux $\tilde{\lambda}_m(k)$ and (33).
- 6) Calculate the magnetizing inductance L_m using (32).
- 7) Update the inductance matrix \mathbf{L} using (14).
- 8) Predict the stator voltages $\underline{v}_{dq}(k)$ using (28).
- 9) Calculate the flux $\underline{\lambda}_{dq}(k)$ using (25).
- 10) Calculate the currents $\underline{i}_{dq}(k)$ and $\underline{i}_{0s}(k)$ using (29) and (30), respectively.
- 11) Calculate $\underline{\lambda}_{md}(k)$ and $\underline{\lambda}_{mq}(k)$ using (36) and (37), respectively; update $\lambda_m(k)$ using (35).
- 12) Calculate the electromagnetic torque $T_e(k)$ using (44); update the electrical rotor speed $\omega_r(k)$ using (45); update the rotor angle $\theta_r(k)$ using (46).
- 13) Calculate the output current $\underline{i}_{Mabcs}(k)$ using (31).
- 14) Calculate the adjustment current source $\underline{i}_{Abcs}(k)$ using (42).
- 15) Return the Norton sources $\underline{i}_{Mabcs}(k)$ and $\underline{i}_{Abcs}(k)$ to the system solver.

H. Machine-Network Solution

The information exchange between the multi-scale model and the system model solver is clarified in Fig. 5. At the beginning

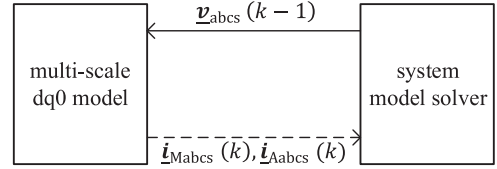


Fig. 5. Information exchange between the multi-scale dq0 model and the system model solver during time-step k .

of step 1 in Section III-G, the multi-scale dq0 model receives its terminal voltages from the system model solver. At the end of step 15 in Section III-G, the multi-scale dq0 model returns information of its Norton sources to the system model solver. The automatic control of shift frequency and time-step size [10] is performed in the system model solver. The shift frequency and time-step size are selected based on signal processing that involves the recursive discrete Fourier transform (RDFT). The system model solver can then proceed with updating the nodal voltages of the system. Upon completion, the algorithm of the multi-scale model introduced in Section III-G starts with step 1 again.

IV. VALIDATION AND TEST SIMULATION

In this paper, three tests are performed to validate the proposed machine model. The proposed machine model is implemented in the simulation method FAST [9] mentioned in Section I. Stationary reference frame is chosen for the induction machine model in the case studies as an example. In Section IV-A, a test system comprising a 50 HP induction machine connected directly to an ideal voltage source is used to examine the results provided by the proposed machine model. The focus of this test system is on the individual machine model. In Section IV-B, a multi-machine test system has been used to further analyze the numerical properties of the proposed machine model. In Section IV-C, a test system consisting of a wound-rotor induction machine and a VSC is used to demonstrate that the proposed machine model is effective in simulating multi-scale transients in the power electronic system.

A. Multiscale Simulation of the Single Machine Model

In this section, a study involving a step increase in the machine's terminal voltage is used to illustrate the saturation phenomenon. Similar case studies have been used in [18], [19] for investigating saturation of synchronous machine and induction machine. Parameters of this particular case are taken from [19] and are summarized in Appendix V-D. The scenario of Table II covers a sequence of diverse stages. The initial transient at $t = 0.2$ s is triggered by a step change in the stator terminal voltages from 100% to 120% of the rated value. Details of how to select the shift frequencies and time-step sizes are elaborated upon in [10] and discussed in the following.

Since the analytical solution is not available, the same study has been simulated using the saturable dq0 model of PSCAD/EMTDC. The model is solved with a very small time-step size of 1 μ s to obtain a very accurate solution. The solution

TABLE II
SETTING OF SHIFT FREQUENCY f_s AND TIME-STEP SIZE τ
IN STUDY OF DIVERSE TRANSIENTS

Time (s)	Stages	f_s (Hz)	τ (s)	f_c (Hz)
0.00-0.20	steady state	60	20e-3	60
0.20-0.27	electromagnetic transient	0	50e-6	60
0.27-0.52	electromechanical transient	60	2e-3	60
0.52-0.80	approaching steady state	60	20e-3	60

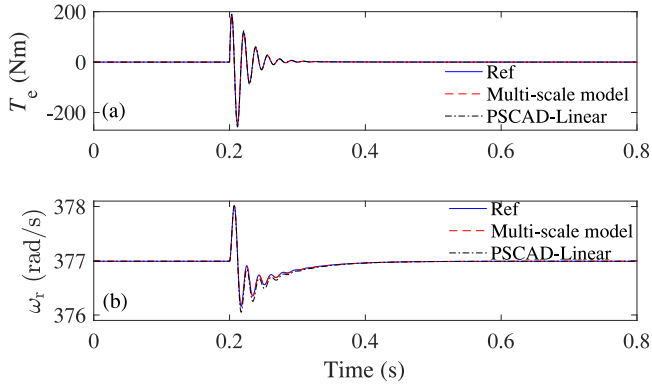


Fig. 6. Multi-scale simulation results for a step change in terminal voltages of a 50 HP induction machine. (a) Electromagnetic torque; (b) machine angular speed; solid: reference solutions, dashed: solutions for the proposed multi-scale model, dash-dotted: solutions for the magnetically-linear model of PSCAD/EMTDC.

obtained by the saturable dq0 model of PSCAD/EMTDC is therefore considered here as a reference for the purpose of comparison. Although the purpose of this analysis is not to show the difference between the saturable and magnetically-linear induction machine models, the magnetically-linear induction machine model of PSCAD/EMTDC is also included in the simulation.

For the scenario of Table II, the electromagnetic torque T_e and the rotor angular speed ω_r are depicted in Fig. 6. The curves of the electromagnetic torque and the rotor angular speed obtained with the multi-scale saturable induction machine model are very close to the reference solution. The stator current i_{as} is depicted in Fig. 7. The curves show how the multi-scale model supports the tracking of both natural and envelope waveforms in one simulation run. To give the reader a better view of the match, zoomed-in views of the stator current i_{as} during diverse stages are shown in Fig. 8, Fig. 9 and Fig. 10, respectively. As shown in these figures, the differences between the linear and saturable models are visible. The stator current of saturable models is higher than that of linear model following the voltage increase.

The simulation starts out in steady state at $t = 0$ s. Envelope waveforms are tracked at the beginning in steady state. The shift frequency f_s is equal to the carrier frequency of 60 Hz and the time-step size τ is equal to 20 ms. At $t = 0.2$ s, the stator terminal voltages are stepped up from 100% to 120% of the rated value. A discontinuity is detected in the proposed model. As a consequence, the simulation parameters are set to $f_s = 0$ Hz and $\tau = 50 \mu s$, natural waveforms are now being tracked since electromagnetic transients are expected. The change from envelope tracking to the tracking of natural waveforms is visible in Fig. 7(a). The RDFT is performed to evaluate spectra of natural

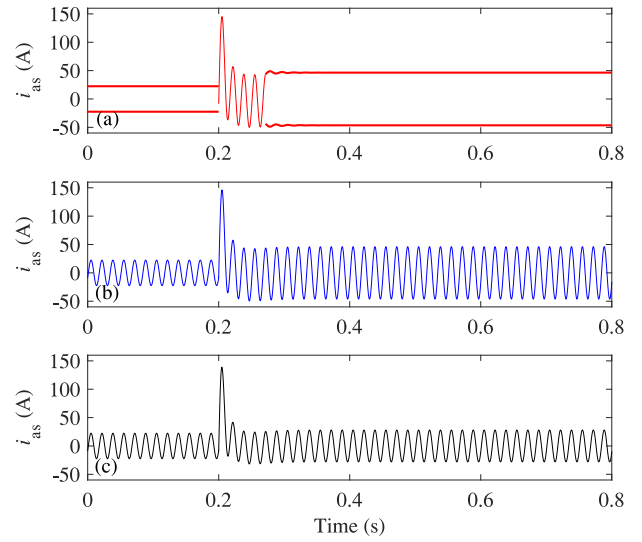


Fig. 7. Phase a stator current i_{as} ; (a) natural and envelope waveforms in the multi-scale simulation; solid light: natural waveform; solid bold: envelope; (b) natural waveform of the reference solution; and (c) natural waveform of the solution for the magnetically-linear model of PSCAD/EMTDC.

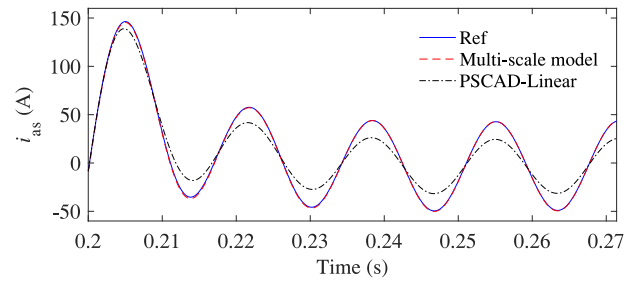


Fig. 8. Zoomed-in view of stator current i_{as} during electromagnetic transients stage.

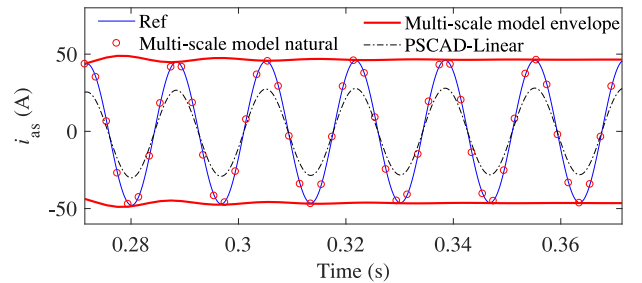


Fig. 9. Zoomed-in view of stator current i_{as} during electromechanical transients stage.

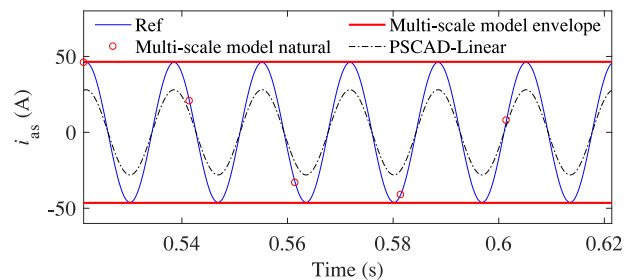


Fig. 10. Zoomed-in view of stator current i_{as} during quasi steady state stage.

TABLE III
SIMULATION ACCURACY OF THE PROPOSED MODEL

Time (s)	Stages	2-norm errors of i_{as} (%)
0.20-0.27	electromagnetic transient	0.7461
0.27-0.52	electromechanical transient	0.2865
0.52-0.80	approaching steady state	0.0638

waveform of stator current i_{as} . At about $t = 0.27$ s, the spectrum is concentrated about 60 Hz, the electromagnetic transients have largely damped out. Remaining electromechanical transients are emulated with envelope tracking at $\tau = 2$ ms and $f_s = 60$ Hz as shown in Fig. 7(a) and Fig. 9. When envelopes are tracked, then the RDFT is performed on the envelope waveform of stator current i_{as} . At about $t = 0.52$ s, the spectrum of envelope waveform drops to low values, e.g., 10 Hz, steady-state conditions approach, a larger time-step size of 20 ms is used. The envelope is tracked further to represent the quasi steady state as shown in Fig. 10.

The proposed multi-scale model processes analytic signals and can so adapt to diverse types of waveforms for an efficient simulation of electromagnetic and electromechanical transients. The envelope information is obtained at the much larger time-step size of 2 ms or 20 ms with the Fourier spectra shifted by $f_s = 60$ Hz leading to fast computations. To investigate the accuracies of envelope waveforms processed by the multi-scale model, the time domain instantaneous values of i_{as} are obtained using the real part of the analytic signals according to (1). The natural waveforms are shown using circles in Fig. 9 and Fig. 10 and they are labeled as “multi-scale model natural”. As observed in Fig. 9 and Fig. 10, the simulation results obtained with the multi-scale model are very close to the reference solutions. Over the entire scenario, there is no noticeable difference in accuracy between solutions produced by the multi-scale model and reference solutions.

Accuracy of the Multi-scale dq0 Machine Model: For evaluating the accuracy of the proposed model, the 2-norm cumulative relative errors of stator current i_{as} are used [29]:

$$\varepsilon(i_{as}) = \frac{\|i_{as,ref} - i_{as}\|_2}{\|i_{as,ref}\|_2} \times 100\%, \quad (48)$$

where i_{as} is the solution trajectory obtained from the proposed model, $i_{as,ref}$ is the reference solution, and $\|i_{as}\|_2$ denotes 2-norm of i_{as} . The 2-norm cumulative relative errors of i_{as} are given in Table III. During electromagnetic transient, a time-step size of $50 \mu\text{s}$ is used, the error is 0.7461%. During stages of electromechanical transient and quasi steady state, much larger time-step sizes are used. The errors during these stages are 0.2865% and 0.0638%, respectively. The proposed multi-scale model provides accurate results over the entire scenario.

To further assess the quality of the proposed multi-scale induction machine model, the study carried out in Section IV-A is repeated with a fixed time-step size of $500 \mu\text{s}$. The saturable induction machine model of PSCAD is included in the comparison. The time-step size in PSCAD/EMTDC is also set to $500 \mu\text{s}$. The stator current i_{as} during the electromagnetic transient is shown in Fig. 11. It can be seen that the proposed multi-scale

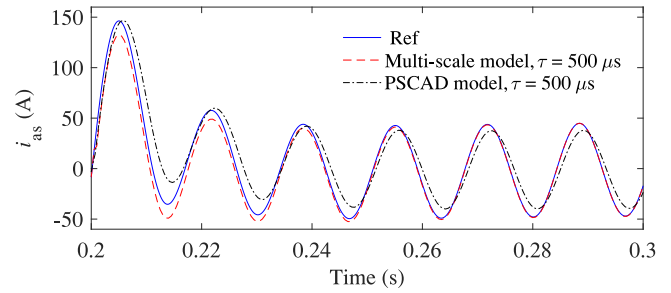


Fig. 11. Phase a stator current i_{as} during electromagnetic transient using a time-step of $500 \mu\text{s}$ for multi-scale model and PSCAD.

TABLE IV
COMPARISON OF CPU TIMES PER TIME-STEP

Models	EMTP-type	Multi-scale	
		$f_s = 0$ Hz	$f_s = f_c$
CPU times per time-step (μs)	1	1.44	1.62

model produces more accurate results than the model of PSCAD. The improved accuracy can be attributed to the prediction of magnetic saturation in Section III-D and the improved interface in Section III-E.

Efficiency of the Multi-scale dq0 Machine Model: To assess the computational speed, the proposed multi-scale dq0 model and an EMTP-type dq0 model that only processes instantaneous signals but otherwise is of equal structure were implemented using standard C language. The models were executed on a personal computer (PC) with an Intel Core i7-7700K, 4.20-GHz processor and 16 GB RAM. The CPU times per time-step required by the two models are summarized in Table IV. The EMTP-type dq0 model makes use of real signals, while the multi-scale dq0 model processes analytic signals. For the proposed multi-scale dq0 model, two cases are considered: the unshifted case of $f_s = 0$ Hz and the shifted case of $f_s = f_c$. When simulating electromagnetic transients, a small time-step size of $50 \mu\text{s}$ is required by both multi-scale dq0 model and EMTP-type dq0 model. For the multi-scale model, the shift frequency is set to $f_s = 0$ Hz. The processing of analytic rather than real signals increases the computational cost by a factor of $(1.44 \mu\text{s})/(1 \mu\text{s}) = 1.44$ per time-step. In the simulation of electromechanical transients, the shift frequency is set equal to the carrier frequency $f_s = f_c$ and the time-step size is set to $\tau = 2$ ms for the multi-scale dq0 model. However, the EMTP-type dq0 model still used a time-step size of $50 \mu\text{s}$. The computational speed of the multi-scale dq0 model was $(2 \text{ ms}) \cdot (1 \mu\text{s}) / (50 \mu\text{s}) / (1.62 \mu\text{s}) \approx 25$ times higher than that of the EMTP-type model. When the machine approaches steady state conditions, the multi-scale dq0 model used a larger time-step of 20 ms. The computational speed of the multi-scale dq0 model was $(20 \text{ ms}) \cdot (1 \mu\text{s}) / (50 \mu\text{s}) / (1.62 \mu\text{s}) \approx 247$ times higher than that of the EMTP-type model.

B. Multiscale Simulation of the Multimachine System

As a second validation step, a multi-machine system is used to analyze the numerical properties of the proposed model. The one-line diagram of the system is depicted in Fig. 12. A

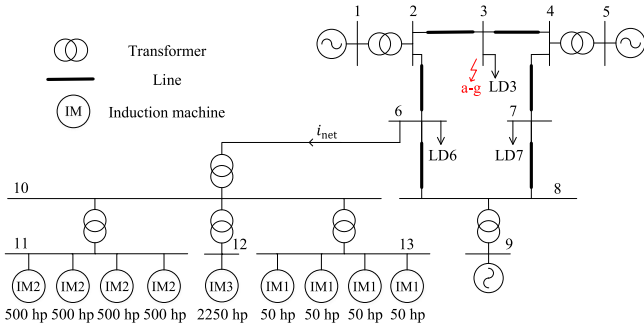


Fig. 12. One-line diagram of the multi-machine power system.

distribution network which comprises 9 induction machines is connected to the WSCC-9 bus system at bus 6. All machine models include main flux saturation. The modeling of lines and transformers can be found in [10]. The parameters of the WSCC-9 bus system are given in [30]. The machine and transformer parameters are summarized in Appendix V-D. The machines initially operate in the steady state. A single-phase to ground fault occurs at bus 3 at $t = 0.1$ s. The fault vanishes 50 ms later before any protection device is activated. As in Section IV-A, this case study also allows the multi-scale simulation. For the purpose of comparison, the network is also modeled using the PSCAD/EMTDC. The simulation of PSCAD remains at a fixed time-step size of $50 \mu\text{s}$.

The curves for the current flowing into the distribution network are shown in Fig. 13. The solution obtained with multi-scale simulation is in close agreement with the reference solution in PSCAD. At the beginning of the simulation, the envelope tracking is used to present the steady state conditions. From $t = 0.1$ s, electromagnetic transients appear due to the occurrence of the fault, and thus natural waveforms need to be tracked. The fast fault transients are simulated with a small time-step size of $50 \mu\text{s}$. By $t = 0.22$ s, the electromagnetic transients have strongly decayed to resume envelope tracking at $f_s = 60$ Hz and $\tau = 2$ ms. From $t = 0.59$ s, as steady-state conditions approach, an increasingly clean sine waveform appears, a larger time-step size of $\tau = 20$ ms is used.

The proposed model shows to accurately simulate diverse transients including the tracking of both natural and envelope waveforms. In order to further investigate the performance, the computational efficiency is compared with that of an EMTP-type implementation of equal structure. Similar comparisons may be found in [10], [11]. In the multi-scale simulation, the analytic signals are used, while the real signals are used for the EMTP-type implementation. In the simulation of electromagnetic transients, both implementations require a comparatively small time-step size, e.g., $50 \mu\text{s}$ in the above example. The processing of analytic rather than real signals has shown to increase the computational cost by a factor of about 1.45. For the electromechanical transients, a larger time-step size of 2 ms may be used in the multi-scale simulation. Taking into account that analytic signals are processed, the computational speed is increased by a factor of $(2 \text{ ms})/(50 \mu\text{s})/1.45 \approx 28$. When the system approaches steady state conditions, the time-step size is increased to 20 ms in the multi-scale simulation. The computational speed is increased by a factor of $(20 \text{ ms})/(50 \mu\text{s})/1.45 \approx 276$. Thus,

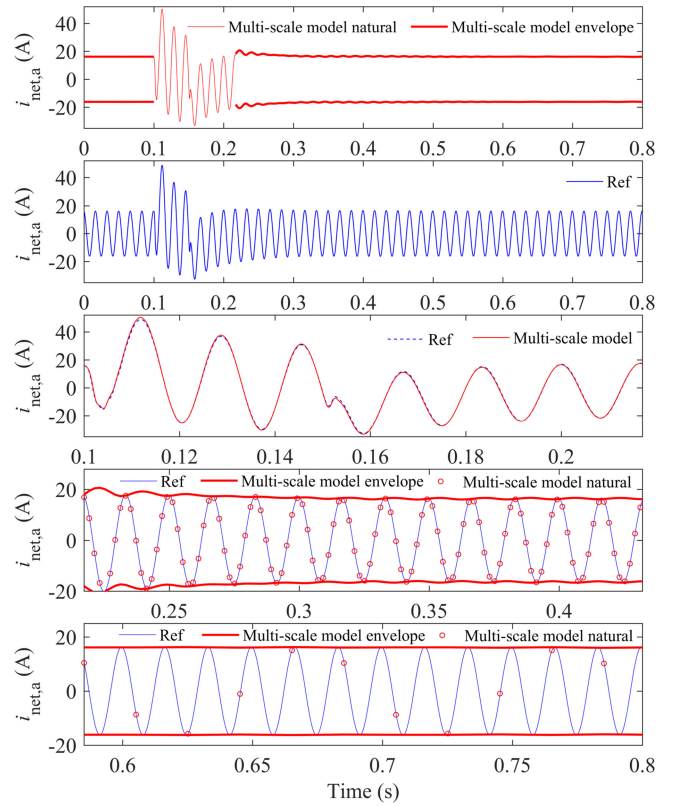


Fig. 13. Phase a current of i_{net} ; (a) natural and envelope waveforms in the multi-scale simulation; solid light: natural waveform; solid bold: envelope; (b) natural waveform of the reference solution in PSCAD; (c) zoomed-in view of $i_{\text{net},a}$ during electromagnetic transients; dashed: natural waveforms of reference solution; solid: natural waveforms in the multi-scale simulation; (d) zoomed-in view of $i_{\text{net},a}$ during electromechanical transients; solid light: natural waveform of the reference solution; solid bold: envelope waveforms in the multi-scale simulation; circle: natural waveforms in the multi-scale simulation; and (e) zoomed-in view of $i_{\text{net},a}$ during quasi steady state; solid light: natural waveform of the reference solution; solid bold: envelope waveforms in the multi-scale simulation; circle: natural waveforms in the multi-scale simulation.

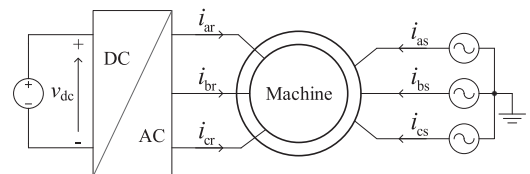


Fig. 14. Diagram of a wound-rotor induction machine controlled by a VSC-based drive system.

for the simulation over longer time intervals, the computational cost is significantly reduced for the period of electromechanical transients and steady states.

C. Multiscale Simulation of the Induction Machine Controlled by a VSC-Based Drive System

In order to further validate the proposed machine model, the test system of Fig. 14 is considered. The stator windings of a 50 HP wound-rotor induction machine are directly connected to an ideal voltage source whose frequency is 60 Hz. The machine rotor windings are connected to a VSC. The machine parameters and the saturation parameters are given in Table VI and Table VII, respectively.

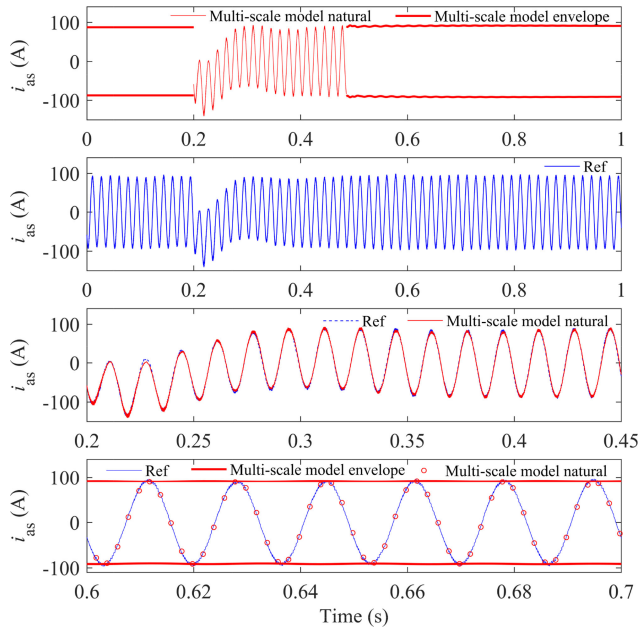


Fig. 15. Phase a stator current i_{as} ; (a) natural and envelope waveforms in the multi-scale simulation; solid light: natural waveform; solid bold: envelope; (b) natural waveform of the reference solution in PSCAD; (c) zoomed-in view of i_{as} during electromagnetic transients; dashed: natural waveforms of reference solution; solid: natural waveforms in the multi-scale simulation; and (d) zoomed-in view of i_{as} during electromechanical transients; solid light: natural waveform of the reference solution; solid bold: envelope waveforms in the multi-scale simulation; circle: natural waveforms in the multi-scale simulation.

The induction machine was represented through the multi-scale induction machine model introduced in Section III. The multi-scale VSC model is a combination of both switching function and averaged models of the VSC [31]. The averaged and switching function models of the VSC are selected depending on the types of transients of interest. The PWM switching frequency is 1800 Hz. The control of the VSC is elaborated upon in Appendix V-E. The test system initially operates in the steady state. At $t = 0.2$ s, the stator terminal voltages of the machine are stepped down from 100% to 80% of the rated value.

For the purpose of comparison, the test system is also simulated with PSCAD/EMTDC. In PSCAD, the switching function VSC model is used. The VSC adopts the PWM strategy with a switching frequency of 1800 Hz. A small time-step size of $10 \mu\text{s}$ is chosen throughout the simulation. The stator current and rotor current of the machine are shown in Fig. 15 and Fig. 16, respectively. It is observed that the results obtained with multi-scale and EMTDC simulations match closely.

At the beginning of the simulation, the system is running in the steady state. As shown in Table V, initially the time-step size is set to 2 ms and the averaged VSC model is adopted. From $t = 0.2$ s, electromagnetic transients appear due to the change in stator voltages of the machine. Then, to get more details, the switching function model of the VSC is chosen. The time-step size is set to $10 \mu\text{s}$, and natural waveforms are tracked. The ripples in the currents do appear as shown in Fig. 15 and Fig. 16. As the electromagnetic transients damp out, the envelope tracking resumes at $t = 0.48$ s, and the averaged model of VSC is adopted.

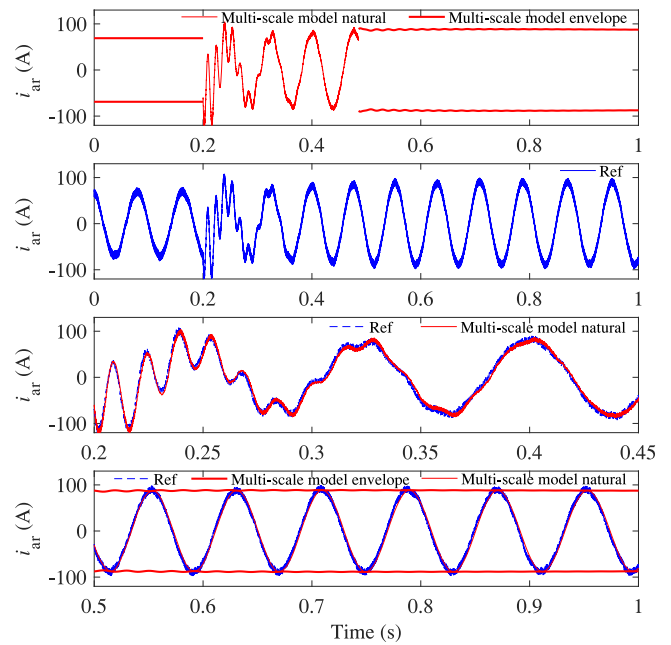


Fig. 16. Phase a rotor current i_{ar} ; (a) natural and envelope waveforms in the multi-scale simulation; solid light: natural waveform; solid bold: envelope; (b) natural waveform of the reference solution in PSCAD; (c) zoomed-in view of i_{ar} during electromagnetic transients; dashed: natural waveforms of reference solution; solid: natural waveforms in the multi-scale simulation; and (d) zoomed-in view of i_{ar} during electromechanical transients; dashed: natural waveform of the reference solution; solid bold: envelope waveforms in the multi-scale simulation; solid light: natural waveforms in the multi-scale simulation.

TABLE V
SETTING OF SHIFT FREQUENCY f_s , TIME-STEP SIZE τ , AND
VSC MODEL IN MULTISCALE SIMULATION

Time (s)	Stages	f_s (Hz)	τ (s)	VSC model
0.00-0.20	steady state	60	2e-3	averaged
0.20-0.48	electromagnetic transient	0	10e-6	switching function
0.48-1.00	electromechanical transient	60	2e-3	averaged

V. CONCLUSION

A multi-scale induction machine model including magnetic saturation in the dq0 domain was developed, implemented, and validated. The electrical quantities are expressed through analytic signals that support frequency shifting of involved Fourier spectra. The prediction of flux linkages as well as the interface between the proposed model and the external network model is improved, thereby providing superior numerical accuracy than the EMTP-type dq0 model when using large time-step sizes.

The performance has been validated through case studies. By comparing with the EMTP-type simulation results, a very high of accuracy was observed. The shift frequency appears as a new parameter in addition to the time-step size. Both shift frequency and time-step size were adapted to the present situation giving diverse transients. If the shift frequency is zero, it is suitable for processing instantaneous signals just as EMTP. If the shift frequency is equal to the carrier frequency, it is more suitable to do simulation with existing dynamic phasors. In sum, the main scientific contribution pertains to the capability of the proposed multi-scale saturable induction machine model to efficiently and

accurately model transients across multiple time scales. Future work would extend the multi-scale saturable induction machine model to consider other formulations and to analyze numerical properties of different types of induction machine models based on frequency shifting.

APPENDIX

A. Basic Equations of Induction Machine in the dq0 Domain

The voltage equations of the full-order machine model in the arbitrary reference frame are given as [23]:

$$v_{ds}(t) = R_s i_{ds}(t) - \omega \lambda_{qs}(t) + \frac{d\lambda_{ds}(t)}{dt}, \quad (49)$$

$$v_{qs}(t) = R_s i_{qs}(t) + \omega \lambda_{ds}(t) + \frac{d\lambda_{qs}(t)}{dt}, \quad (50)$$

$$v_{dr}(t) = R_r i_{dr}(t) - (\omega - \omega_r) \lambda_{qr}(t) + \frac{d\lambda_{dr}(t)}{dt}, \quad (51)$$

$$v_{qr}(t) = R_r i_{qr}(t) + (\omega - \omega_r) \lambda_{dr}(t) + \frac{d\lambda_{qr}(t)}{dt}. \quad (52)$$

The voltage equations (49), (50), (51), and (52) can be written in matrix form as shown in (3).

The flux linkages may be expressed as follows:

$$\lambda_{ds}(t) = L_{ls} i_{ds}(t) + \lambda_{md}(t), \quad (53)$$

$$\lambda_{qs}(t) = L_{ls} i_{qs}(t) + \lambda_{mq}(t), \quad (54)$$

$$\lambda_{dr}(t) = L_{lr} i_{dr}(t) + \lambda_{md}(t), \quad (55)$$

$$\lambda_{qr}(t) = L_{lr} i_{qr}(t) + \lambda_{mq}(t), \quad (56)$$

with

$$\lambda_{md}(t) = L_m (i_{ds}(t) + i_{dr}(t)), \quad (57)$$

$$\lambda_{mq}(t) = L_m (i_{qs}(t) + i_{qr}(t)). \quad (58)$$

The flux equations (53), (54), (55), and (56) can be written in matrix form as shown in (11).

B. Prediction With Analytic Signals

Let an ac source voltage with $\hat{v}_e = 1$ V be described by the following excitation function:

$$v_e(t) = \hat{v}_e \sin(2\pi 60t). \quad (59)$$

By adding a quadrature component as an imaginary part through the Hilbert transform, an analytic signal is then obtained:

$$\underline{v}_e(t) = \hat{v}_e e^{(j2\pi 60t - j\frac{\pi}{2})}. \quad (60)$$

It is assumed that the voltage v_e at $t - \tau$ is known and that the voltage at t is to be found.

Prediction based on analytic signals gives:

$$\tilde{v}_e(t) = e^{j2\pi 60\tau} \underline{v}_e(t - \tau). \quad (61)$$

The results of the predictions are shown in Fig. 17 for $\tau = 2$ ms. For comparison, the linear extrapolations $\tilde{v}_e(t) = 2v_e(t - \tau) - v_e(t - 2\tau)$ are also shown. For the given sinusoidal waveform, (61) gives better results.

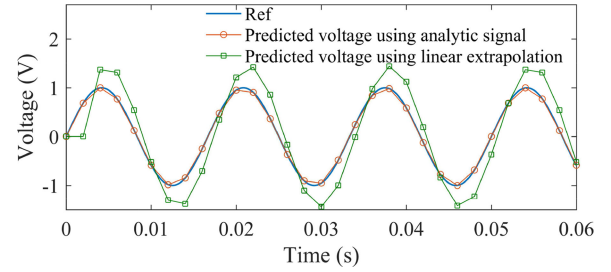


Fig. 17. Predictions of voltage $v_e(t)$ using a time-step size of 2 ms.

TABLE VI
PARAMETERS OF INDUCTION MACHINES

Symbol (unit)	Quantity	IM1	IM2	IM3
P_{rated} (hp)	rated power	50	500	2250
V_n (kV)	line to line voltage	0.46	2.3	2.3
R_s (Ω)	stator resistance	0.087	0.262	0.029
R_r (Ω)	rotor resistance	0.228	0.187	0.022
$X_{m,unsat}$ (Ω)	unsaturated magnetizing reactance	13.08	54.02	13.04
X_{ls} (Ω)	stator leakage reactance	0.302	1.206	0.226
X_{lr} (Ω)	rotor leakage reactance	0.302	1.206	0.226
J ($\text{kg} \cdot \text{m}^2$)	inertia of machine	1.662	11.06	63.87
p	number of poles	4	4	4

TABLE VII
SATURATION PARAMETERS OF INDUCTION MACHINES

	IM1		IM2		IM3	
λ_m (Wb)	0.80	1.00	3.95	4.80	3.95	4.80
i_m (A)	23.06	52.05	27.57	54.29	114.16	224.90

C. Reference-Frame Transformation

Let variables $\mathbf{X}_{dq0} = (X_d \ X_q \ X_0)^T$ be represented in an arbitrary reference frame rotating at speed ω and where the q-axis leads the d-axis by 90° . The transform from phase variables $\mathbf{X}_{abc} = (X_a \ X_b \ X_c)^T$ to the arbitrary reference frame is [23]:

$$\mathbf{X}_{dq0} = \mathbf{K}(\theta) \mathbf{X}_{abc} \quad (62)$$

with

$$\mathbf{K}(\theta) = \frac{2}{3} \begin{bmatrix} \cos \theta & \cos(\theta - \frac{2\pi}{3}) & \cos(\theta + \frac{2\pi}{3}) \\ -\sin \theta & -\sin(\theta - \frac{2\pi}{3}) & -\sin(\theta + \frac{2\pi}{3}) \\ \frac{1}{2} & \frac{1}{2} & \frac{1}{2} \end{bmatrix}, \quad (63)$$

$$\frac{d\theta}{dt} = \omega - \omega_{ph} \quad (64)$$

where ω_{ph} denotes the rotational speed of the abc reference frame. It is assumed here that at $t = 0$ s, the d-axis and a-axis coincide.

D. Parameters of Test Systems

The induction machine parameters are taken from [23] and given in Table VI. Following the approach used in [19], the saturation characteristics of induction machines are represented by using the two-slope piecewise-linear method. The saturation parameters are given in Table VII. The saturation parameters of induction machine IM1 are taken from [19]. The saturation

- [28] F. Gao and K. Strunz, "Multi-scale simulation of multi-machine power systems," *Int. J. Elect. Power Energy Syst.*, vol. 31, no. 9, pp. 538–545, Oct. 2009.
- [29] W. Gautschi, *Numerical Analysis: An Introduction*. Boston, MA, USA: Birkhauser, 1997.
- [30] P. M. Anderson and A. A. Fouad, *Power System Control and Stability*. Piscataway, NJ, USA: IEEE Press, 1994.
- [31] H. Ye, B. Yue, X. Li, and K. Strunz, "Modeling and simulation of multi-scale transients for PMSG-based wind power systems," *Wind Energy*, vol. 20, no. 1, pp. 1349–1364, Mar. 2017.
- [32] A. Yazdani and R. Iravani, *Voltage-Sourced Converters in Power Systems: Modeling, Control, and Applications*. Hoboken, NJ, USA: Wiley, 2010.
- [33] R. Pena, and J. C. Clare, and G. M. Asher, "Doubly fed induction generator using back-to-back PWM converters and its application to variable-speed wind-energy generation," *Proc. Inst. Elect. Eng. B*, vol. 143, no. 3, pp. 231–241, May 1996.



Yue Xia received the B.S. and M.S. degrees in electrical engineering from the China Agricultural University, Beijing, China, in 2009 and 2011, respectively. He received the Ph.D. degree in electrical engineering from the Technische Universität Berlin, Germany, in 2016.

He is currently working as a Postdoctoral with the Department of Electrical Engineering and Applied Electronic Technology, Tsinghua University, Beijing, China. His research interests include power electronic systems, electrical machines, wind power, and modeling and simulation of power system transients.



Ying Chen (M'07) received the B.E. and Ph.D. degrees in electrical engineering from Tsinghua University, Beijing, China, in 2001 and 2006, respectively.

He is currently an Associate Professor with the Department of Electrical Engineering and Applied Electronic Technology, Tsinghua University, Beijing, China. His research interests include parallel and distributed computing, electromagnetic transient simulation, cyber-physical system modeling, and cyber security of smart grids.



Hua Ye received the B.S. and M.S. degrees in electrical engineering from the China Agricultural University, Beijing, China, in 2006 and 2008, respectively, and the Ph.D. degree in electrical engineering from the Technische Universität Berlin, Germany, in 2013.

He is currently an Associate Professor with the Institute of Electrical Engineering, Chinese Academy of Sciences, Beijing, China. His research interests include modeling of power system transients, computational methods, integration of wind power, and HVDC grids.



Kai Strunz received the Dipl.Ing. and Dr. Ing. degrees (*summa cum laude*) from the Saarland University, Saarbrücken, Germany, in 1996 and 2001, respectively.

He was with Brunel University, London, U.K., from 1995 to 1997. From 1997 to 2002, he was with the Division Recherche et Développement of Electricité de France, Paris, France. From 2002 to 2007, he was an Assistant Professor in electrical engineering with the University of Washington, Seattle, WA, USA. Since 2007, he is a Professor for Sustainable

Electric Networks and Sources of Energy with Technische Universität (TU) Berlin, Berlin, Germany.

Dr. Strunz was the Chairman of the Conference IEEE PES Innovative Smart Grid Technologies, TU Berlin, in 2012. He is a Chairman of the IEEE Power and Energy Society Subcommittee on Distributed Energy Resources and Past Chairman of the Subcommittee on Research in Education. On behalf of the Intergovernmental Panel on Climate Change, he acted as a Review Editor for the Special Report on Renewable Energy Sources and Climate Change Mitigation. He was the recipient of the IEEE PES Prize Paper Award in 2015 and the Journal of Emerging and Selected Topics in Power Electronics First Prize Paper Award 2015.